

ChimeraLM detects amplification artifacts for
accurate structural variant calling in long-read
single-cell sequencing

Yangyang Li^{1†}, Qingxiang Guo^{1†}, Rendong Yang^{1,2*}

¹Department of Urology, Northwestern University Feinberg School of Medicine, 303 E Superior St, Chicago, 60611, IL, USA.

²Robert H. Lurie Comprehensive Cancer Center, Northwestern University Feinberg School of Medicine, 675 N St Clair St, Chicago, 60611, IL, USA.

*Corresponding author(s). E-mail(s): rendong.yang@northwestern.edu;
Contributing authors: yangyang.li@northwestern.edu;

qingxiang.guo@northwestern.edu;

†These authors contributed equally to this work.

Abstract

Single-cell genomics enables unprecedented insights into cellular heterogeneity across cancer, development, and neuroscience, but faces a fundamental challenge: Whole Genome Amplification (WGA) introduces chimeric artifacts that generate false Structural Variations (SVs), undermining biological interpretations. Current computational methods fail to distinguish these amplification-induced artifacts from genuine genomic rearrangements. Here we present ChimeraLM, a genomic language model that resolves this bottleneck by learning sequence-level features that discriminate authentic biological sequences from WGA artifacts. Built on Hyena operators for efficient long-range modeling, ChimeraLM analyzes nanopore sequencing reads at single-nucleotide resolution, achieving 95% recall with 70% precision on held-out test data. When applied to WGA-amplified cells, ChimeraLM reduces chimeric read content by ~90% (from 46% to 4.9% on PromethION, 23% to 1.5% on MinION) while preserving 87–92% of true SVs. This filtering improves SV validation rates 10–16 fold and eliminates the characteristic false-positive inversion (INV) bias inherent to unprocessed WGA data, restoring SV type distributions to bulk-like profiles. Attention weight visualization reveals that ChimeraLM focuses on chimeric junction regions with

047 single-base precision, learning biologically interpretable features of template-
048 switching events. By enabling confident detection of chromosomal instability and
049 structural variation at single-cell resolution, ChimeraLM addresses a fundamen-
050 tal data quality barrier across applications in cancer genomics, developmental
051 biology, and precision medicine. The model is available at <https://github.com/ylab-hi/ChimeraLM>.
052

053 **Keywords:** Whole Genome Amplification, Single Cell, Genomic Language Model,
054 Structural Variation

055

056

057

058 Main

059

060 Single-cell genomics has revolutionized our understanding of cellular heterogeneity
061 by enabling characterization of individual cells rather than bulk populations [1–4],
062 revealing previously hidden biological complexity. This approach has proven instru-
063 mental in uncovering rare cell types [4], tracking developmental trajectories [3], and
064 elucidating tumor evolution through clonal architecture analysis. However, the limited
065 DNA content in a single cell—typically only 6–7 picograms containing approximately
066 two copies of the 3-billion-base-pair human genome—poses significant technical chal-
067 lenges for comprehensive genomic analysis [5–7]. To overcome this limitation, **WGA**
068 has become essential for single-cell genomic studies [4, 7–10]. Various **WGA** techniques
069 have been developed, each with distinct amplification mechanisms and characteris-
070 tic error profiles. **Multiple Displacement Amplification (MDA)**, introduced by Dean
071 et al. [10], utilizes the highly processive phi29 DNA polymerase to achieve isother-
072 mal amplification with products exceeding 10 kb, though it suffers from pronounced
073 amplification bias and chimera formation [11, 12]. **Degenerate Oligonucleotide-Primed**
074 **PCR (DOP-PCR)**, pioneered by Telenius et al. [13], employs thermocycling with
075 degenerate primers to achieve more uniform coverage but generates shorter amplicons.
076 **Multiple Annealing and Looping-based Amplification Cycles (MALBAC)** combines
077 quasi-linear preamplification with exponential amplification to reduce bias [8], while
078 **Linear Amplification via Transposon Insertion (LIANTI)** uses transposon insertion
079 to create defined amplification origins, significantly improving uniformity and reduc-
080 ing artifacts [7]. More recently, **Primary Template-directed Amplification (PTA)** [14]
081 and **droplet-based MDA (dMDA)** [15, 16] have emerged as promising alternatives
082 that modify reaction conditions to suppress chimera formation, though these meth-
083 ods require specialized equipment and protocols that have limited their widespread
084 adoption. These amplification methods can increase DNA content by several orders
085 of magnitude (typically 1,000- to 10,000-fold), generating sufficient material for high-
086 coverage sequencing necessary for reliable variant calling, copy number analysis, and
087 **SV** detection [4, 17–21].

088 Accurate single-cell genomics is particularly critical for multiple applications where
089 false-positive **SVs** can lead to incorrect biological conclusions. In cancer research, dis-
090 tinguishing genuine clonal evolution patterns from amplification artifacts is essential
091
092

for understanding tumor heterogeneity and therapeutic resistance [3]. In developmental biology, accurate detection of somatic mosaicism enables the reconstruction of lineage relationships and identification of pathogenic mutations in rare cell populations. For CRISPR-based genome editing, single-cell analysis with reliable SV detection is crucial for comprehensive assessment of off-target effects and ensuring genomic stability [14]. However, false-positive SVs introduced during amplification can confound these analyses, leading to misinterpretation of genomic rearrangements and their biological significance [4, 22].	093
	094
	095
	096
	097
	098
	099
	100
Despite its critical role, WGA introduces systematic artifacts that significantly impact downstream analyses [7, 11, 12, 22, 23]. Chief among these are chimeric sequences—artificial DNA constructs formed through template switching during amplification. During MDA , the highly processive phi29 polymerase can dissociate from one genomic template and reinitiate synthesis on another, creating chimeric molecules that join DNA fragments from distant genomic loci into single amplified products [11]. These artifacts are particularly problematic for long-read sequencing technologies, where chimeric reads can span tens of kilobases and produce convincing—but false—evidence for genomic rearrangements.	101
	102
	103
	104
	105
	106
	107
	108
	109
Current computational tools to detect SVs from long-read data, including Sniffles2 [24, 25], DeBreak [26], SVIM [27], and cuteSV [28]. These methods typically employ read alignment analysis, split-read detection, and local assembly strategies to identify SV signatures [29]. However, distinguishing genuine biological SVs from WGA -induced chimeric artifacts remains challenging [23, 30–32].	110
	111
	112
	113
	114
Current computational approaches for identifying WGA -induced artifacts rely primarily on coverage-based metrics and read-pair orientation patterns [23, 30]. However, these heuristic methods often fail to distinguish genuine SVs from amplification artifacts, particularly when chimeric sequences exhibit complex rearrangement patterns, occur in repetitive genomic regions, or involve multiple genomic loci [31, 32]. This lack of robust, automated artifact detection has limited the reliability of SV analysis in single-cell studies and hindered the full realization of single-cell genomics' potential for studying somatic mosaicism, tumor evolution, and rare cell populations.	115
	116
	117
	118
	119
	120
	121
	122
The emergence of deep learning, particularly language models based on transformer architectures, has demonstrated remarkable success in genomics applications [33–36]. Recent genomic language models have shown the ability to learn complex sequence patterns and contextual relationships in DNA sequences, enabling improved performance in tasks such as regulatory element prediction, variant effect prediction, and functional annotation [36–38]. These models treat DNA sequences analogously to natural language, learning representations that capture both local motifs and long-range dependencies [33]. By training on large-scale genomic datasets, such models can internalize patterns of genuine biological sequences, including characteristic features of repetitive elements, chromatin structure, and sequence composition biases.	123
	124
	125
	126
	127
	128
	129
	130
	131
	132
Here, we developed ChimeraLM, a genomic language model specifically designed to detect chimeric artifacts introduced by WGA . By leveraging deep learning to capture sequence patterns, structural features, and contextual information in genomic reads [33–36, 38], ChimeraLM effectively distinguishes genuine biological sequences from WGA -induced chimeric artifacts. We demonstrate that ChimeraLM achieves	133
	134
	135
	136
	137
	138

139 superior performance compared to existing methods and substantially improves the
140 reliability of **SV** detection in single-cell genomic studies, thereby enabling accurate SV
141 analysis at single-cell resolution.

142

143 **Results**

144

145 **Overview of ChimeraLM workflow and model architecture**

146

147 Single-cell genomics relies on **WGA** to obtain sufficient DNA for sequencing (Fig. 1a).
148 The standard workflow includes single-cell isolation, DNA extraction, **WGA**, long-read
149 sequencing (e.g., **Oxford Nanopore Technologies (ONT)**), base calling, and alignment
150 to the reference genome. During amplification, template-switching events introduce
151 artificial chimeric reads, resulting in alignment files that contain a mixture of authentic
152 and artificial sequences. In downstream analysis, these artifacts can mimic **SV** and
153 confound variant detection. To address this challenge, we developed ChimeraLM, a
154 **Genomic Language Model (GLM)** designed to integrate directly into this analysis
155 pipeline and distinguish biological reads from amplification-induced artifacts.

156 ChimeraLM functions as a pre-processing filter, operating after read alignment
157 but before **SV** detection. It evaluates each chimeric read—sequences with multiple
158 alignments to distant genomic locations—and classifies it as either biological (genuine)
159 or artificial (**WGA**-induced). This binary decision enables the retention of authentic
160 genomic sequences while removing amplification artifacts prior to variant calling. The
161 resulting high-confidence biological reads are then passed to conventional **SV** detection
162 algorithms for accurate identification of genomic rearrangements.

163 A high-confidence labeled dataset was required for supervised training of the model
164 (Fig. 1b; Extended Data Fig. 1a). We constructed this dataset using sequencing data
165 from the PC3 prostate cancer cell line, which provides both **WGA**-amplified and
166 non-amplified (bulk) genomic data. The key assumption is that bulk sequencing con-
167 tains only genuine genomic sequences, whereas **WGA** data includes both genuine and
168 artificial chimeras. Chimeric reads from the PC3 **WGA** PromethION dataset were sys-
169 tematically compared against three independent bulk datasets (**ONT** PromethION,
170 **ONT** MinION, and PacBio; see **Methods**). **WGA** reads whose chimeric structures were
171 absent from all three bulk datasets were labeled artificial. Conversely, **WGA** reads
172 with structures validated in one or more bulk datasets were labeled biological.

173 Application of this labeling strategy to the PC3 **WGA** data (Extended Data
174 Table 1) quantified the read distribution across these categories (Extended Data
175 Fig. 1b). We identified 12,670,396 chimeric reads with zero matches in the bulk ref-
176 erence, which were classified as artificial. Conversely, we identified a total of 293,180
177 reads validated as biological. This biological set was composed of reads matching one
178 (Match 1: 101,094 reads), two (Match 2: 190,309 reads), or all three (Match 3: 1,777
179 reads) of the bulk reference datasets. To construct a balanced training dataset, we
180 retained all 293,180 biological reads (combining Match 1, 2, and 3) and subsampled
181 an equal number (293,180) of artificial reads from the no-match category. This set was
182 augmented with 178,748 chimeric reads subsampled from the bulk datasets as pos-
183 tive controls. The final dataset of 765,108 labeled reads was partitioned into training
184 (70%), validation (20%), and internal test (10%) sets using stratified splitting.

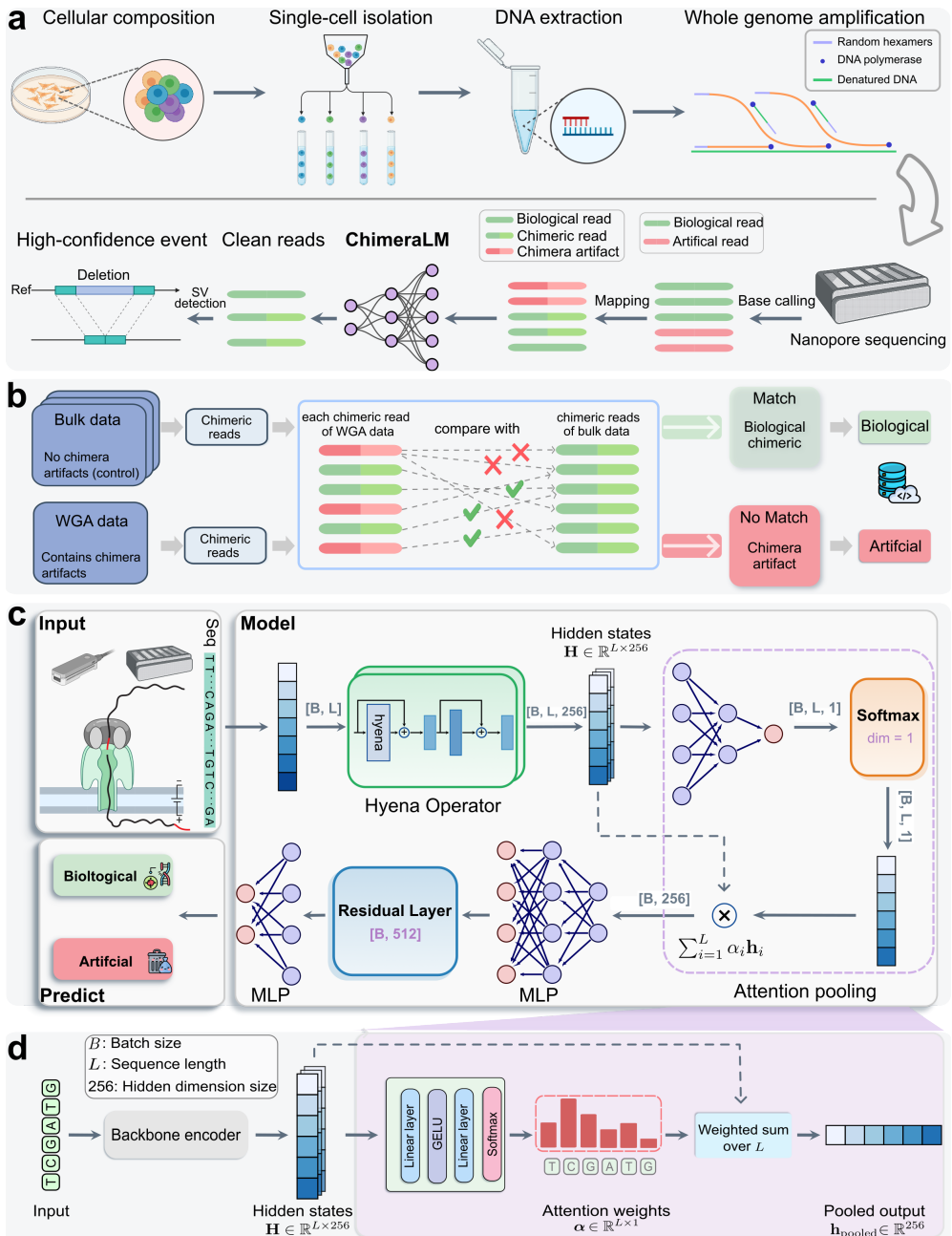


Fig. 1 ChimeraLM workflow and architecture for detecting WGA artifacts in single-cell sequencing. (a) Single-cell genomic workflow and ChimeraLM integration. Single cells are isolated, followed by DNA extraction and WGA for genome amplification. WGA generates chimeric artifacts (red) through template switching during amplification, alongside biological reads (green). After nanopore sequencing, ChimeraLM classifies chimeric reads as biological or artificial, enabling downstream SV detection on clean reads. (b) Ground truth label generation for supervised learning. Chimeric reads from WGA data are compared against all chimeric reads from bulk sequencing data of the same cell line. Reads that match bulk data are labeled as biological (green pathway), while non-matching reads are labeled as chimera artifacts (red pathway). This provides reliable training labels. (c) ChimeraLM architecture. Input DNA sequences (batch size B , sequence length L) are tokenized and encoded into hidden states $H \in \mathbb{R}^{L \times 256}$ through a backbone encoder (HyenaDNA [35]). Hyena operators capture long-range dependencies in genomic sequences. Attention pooling aggregates position-specific features using learned weights. Residual and multilayer perceptron (MLP) layers process pooled features, and a softmax layer outputs binary classification probabilities for biological versus artificial reads. (d) Attention pooling mechanism detail. The backbone encoder (HyenaDNA) transforms input sequences into hidden state $H \in \mathbb{R}^{L \times 256}$. Attention weights $\alpha \in \mathbb{R}^{L \times 1}$ are computed through linear layers, GELU activation, and softmax normalization, assigning importance scores to each nucleotide position. The weighted sum $h_{\text{pooled}} = \sum_{i=1}^L \alpha_i h_i$ produces the pooled output $h_{\text{pooled}} \in \mathbb{R}^{256}$, compressing variable-length sequences into fixed-dimensional representations. Created with BioRender.com.

231 The architecture of ChimeraLM (Fig. 1c) was specifically designed to learn
232 from this dataset by operating directly on raw DNA sequences, bypassing conven-
233 tional, feature-based classifiers. This design must address three primary technical
234 challenges: (1) efficiently processing variable-length sequences of many kilobases,
235 (2) simultaneously maintaining single-nucleotide resolution to detect the precise,
236 abrupt compositional changes that define chimeric junctions, and (3) aggregating
237 variable-length sequence representations into a consistent classification output.

238 ChimeraLM first addresses the need for high resolution by tokenizing input
239 sequences at the single-nucleotide level. This base-pair precision is required to preserve
240 the complete sequence information necessary for detecting chimeric junctions—the
241 breakpoints where disparate genomic regions are artificially fused and which often
242 exhibit abrupt compositional changes.

243 The architecture’s core employs Hyena operators [39], selected specifically to
244 overcome the challenge of processing long DNA sequences. Traditional attention
245 mechanisms scale quadratically with sequence length, making them computationally
246 prohibitive for long-read data. Hyena operators, by contrast, achieve subquadratic
247 scaling, enabling ChimeraLM to analyze full-length reads without fragmentation and
248 thus preserve the structural context around chimeric junctions. To leverage existing
249 genomic knowledge, we initialized the model with weights from HyenaDNA [35], a
250 genomic foundation model pre-trained on diverse DNA sequences.

251 Finally, to produce a classification, the model employs an attention pooling mech-
252 anism to aggregate information across the entire variable-length read (Fig. 1d). This
253 module computes learned, position-specific weights to identify which nucleotides—such
254 as those at the junction boundary—are most informative for the classification deci-
255 sion. This weighted aggregation produces a fixed-dimensional representation, which
256 is then processed through MLP components with residual connections. A final soft-
257 max layer outputs the probability scores for the biological versus artificial classes (see
258 Methods). This end-to-end architecture enables ChimeraLM to learn directly from
259 raw sequence data, discovering complex patterns that may not be apparent through
260 rule-based algorithms.

261

262 **ChimeraLM achieves high accuracy and reduces artifacts to 263 near-bulk levels across platforms**

264

265 We first evaluated ChimeraLM’s classification accuracy on the held-out test set
266 (derived from the PromethION training data), which comprised reads with known bio-
267 logical or artificial status (Fig. 2a). The model achieved an F1 score of 0.81, reflecting
268 balanced sensitivity and specificity in artifact detection. A recall of 0.95 indicates that
269 95% of true chimeric reads were correctly identified—critical for minimizing down-
270 stream false-positive structural variant calls—while a precision of 0.70 shows that the
271 majority of reads flagged as chimeric were true artifacts. These results establish the
272 model’s reliability for identifying amplification-induced artifacts in long-read data.

273 We next assessed its practical effectiveness on the full PC3 WGA datasets, com-
274 paring performance on the PromethION and MinION platforms (Fig. 2b). Bulk
275 sequencing established a low baseline chimeric read rate (2.3% for PromethION; 2.5%
276 for MinION). WGA dramatically increased this artifact load to 46.0% (PromethION)

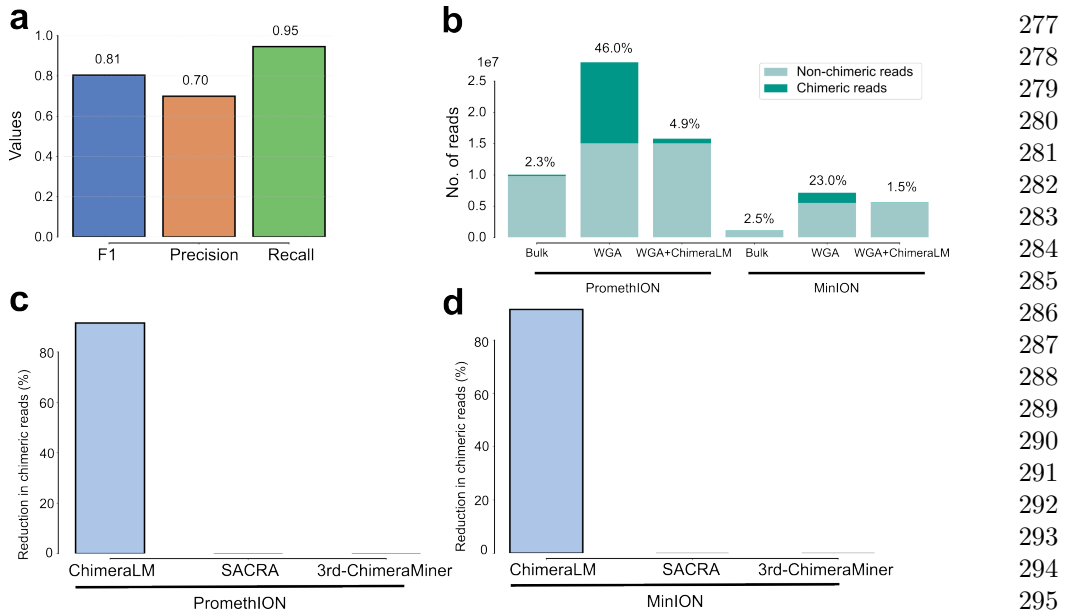


Fig. 2 ChimeraLM accurately identifies and removes WGA-induced chimeric artifacts.

(a) Classification performance on held-out test data. ChimeraLM achieves high recall (0.95) in identifying chimera artifacts while maintaining acceptable precision (0.70), yielding an F1 score of 0.81 for binary classification of biological versus artificial sequences. (b) Chimeric read reduction across sequencing platforms. Stacked bars show the proportion of chimeric (dark teal) and non-chimeric (light teal) reads in bulk sequencing, WGA-amplified samples, and ChimeraLM-filtered WGA samples. Data from PC3 cell line sequenced on PromethION (left) and MinION (right) platforms demonstrate that ChimeraLM reduces chimeric read frequencies from 46.0% to 4.9% (PromethION) and from 23.0% to 1.5% (MinION), approaching bulk levels (2.3% and 2.5%, respectively). (c,d) Benchmarking against existing methods. ChimeraLM achieves approximately 90% reduction in chimeric reads on both PromethION (c) and MinION (d) platforms, whereas existing computational tools SACRA and 3rd-ChimeraMiner show no detectable reduction in chimeric content.

and 23.0% (MinION). After ChimeraLM filtering, chimeric content dropped to 4.9% on PromethION and 1.5% on MinION—representing 10- to 15-fold reductions—while retaining 15.8 million and 5.6 million biological reads. This restoration to near-bulk quality demonstrates that ChimeraLM effectively separates genuine genomic reads from WGA-induced artifacts.

We then benchmarked ChimeraLM against existing computational tools for detecting amplification-induced chimeras, SACRA [30] and 3rd-ChimeraMiner [23] (Fig. 2c,d). When applied to the same PromethION and MinION WGA data, ChimeraLM achieved an approximately 90% reduction in chimeric reads on both platforms. In stark contrast, neither SACRA nor 3rd-ChimeraMiner showed any detectable reduction in chimeric content (0% reduction).

Together, these results demonstrate a robust and generalizable performance. The strong filtering on the MinION dataset (Fig. 2b) is particularly noteworthy, as this dataset served as a completely independent test set; the model was trained exclusively on PromethION data. This cross-platform generalization, combined with the

277
278
279
280
281
282
283
284
285
286
287
288
289
290
291
292
293
294
295
296
297
298
299
300
301
302
303
304
305
306
307
308
309
310
311
312
313
314
315
316
317
318
319
320
321
322

323 high recall on the internal test set (Fig. 2a) and the clear superiority over existing tools
324 (Fig. 2c,d), indicates that ChimeraLM learns fundamental, generalizable sequence
325 features of WGA-induced artifacts rather than platform-specific signatures.

326

327

328

329

330

331

332

333

334

335

336

337

338

339

340

341

342

343

344

345

346

347

348

349

350

351

352

353

354

355

356

357

358

359

360

361

362

363

364

365

366

367

368

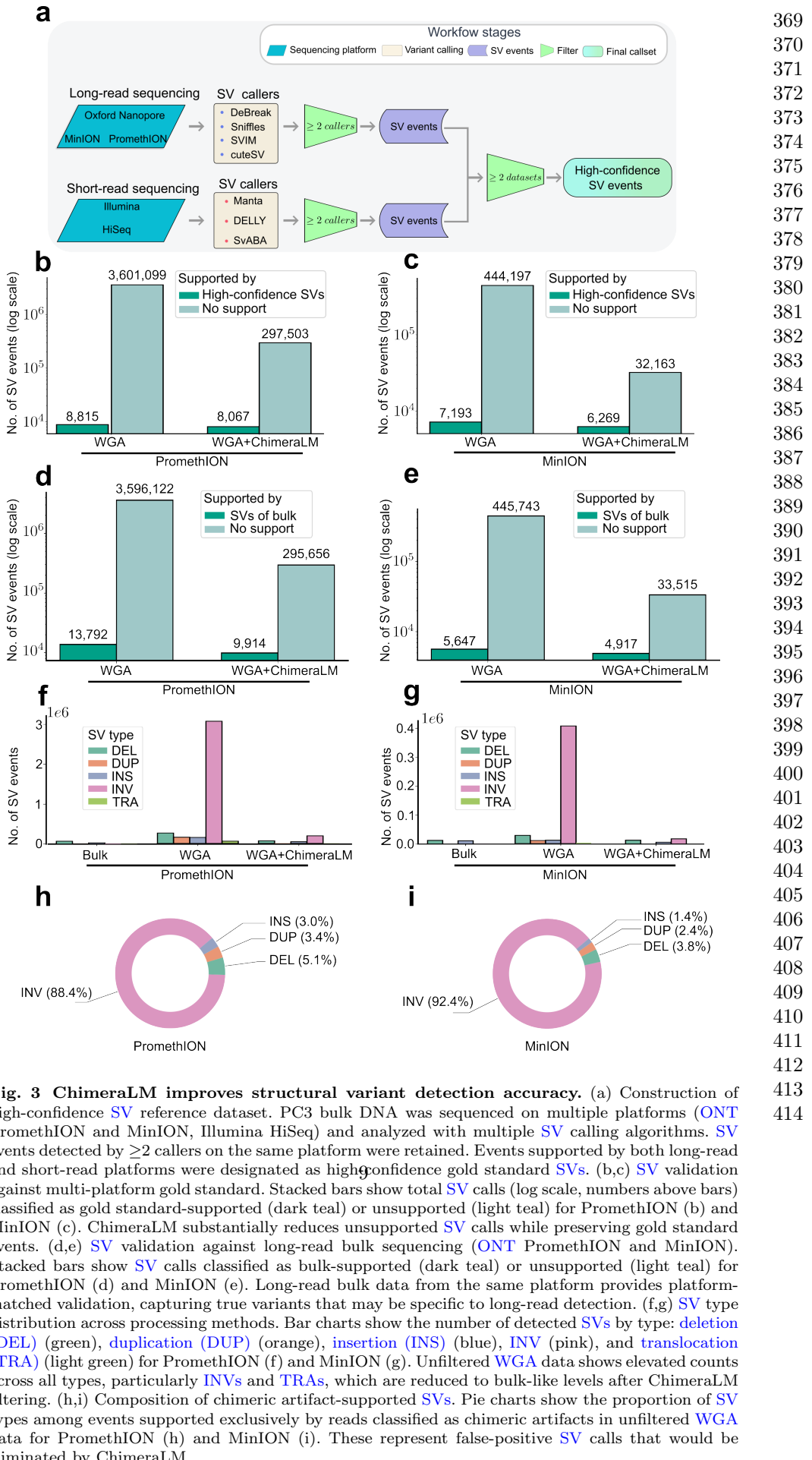


Fig. 3 ChimeraLM improves structural variant detection accuracy. (a) Construction of high-confidence SV reference dataset. PC3 bulk DNA was sequenced on multiple platforms (ONT PromethION and MinION, Illumina HiSeq) and analyzed with multiple SV calling algorithms. SV events detected by ≥2 callers on the same platform were retained. Events supported by both long-read and short-read platforms were designated as high-confidence gold standard SVs. (b,c) SV validation against multi-platform gold standard. Stacked bars show total SV calls (log scale, numbers above bars) classified as gold standard-supported (dark teal) or unsupported (light teal) for PromethION (b) and MinION (c). ChimeraLM substantially reduces unsupported SV calls while preserving gold standard events. (d,e) SV validation against long-read bulk sequencing (ONT PromethION and MinION). Stacked bars show SV calls classified as bulk-supported (dark teal) or unsupported (light teal) for PromethION (d) and MinION (e). Long-read bulk data from the same platform provides platform-matched validation, capturing true variants that may be specific to long-read detection. (f,g) SV type distribution across processing methods. Bar charts show the number of detected SVs by type: deletion (DEL) (green), duplication (DUP) (orange), insertion (INS) (blue), INV (pink), and translocation (TRA) (light green) for PromethION (f) and MinION (g). Unfiltered WGA data shows elevated counts across all types, particularly INVs and TRAs, which are reduced to bulk-like levels after ChimeraLM filtering. (h,i) Composition of chimeric artifact-supported SVs. Pie charts show the proportion of SV types among events supported exclusively by reads classified as chimeric artifacts in unfiltered WGA data for PromethION (h) and MinION (i). These represent false-positive SV calls that would be eliminated by ChimeraLM.

415 **ChimeraLM substantially reduces false-positive structural
416 variant calls**

417 Accurate **SV** detection is essential for understanding genomic diversity and dis-
418 ease mechanisms in single cells. However, **WGA**-induced chimeric artifacts can be
419 misidentified as genuine **SVs**, leading to incorrect biological conclusions. To quantify
420 ChimeraLM’s impact on **SV** calling accuracy, we compared variant calls from unfiltered
421 **WGA** data and ChimeraLM-filtered data against two independent reference standards
422 (Fig. 3).

423 We first established a high-confidence gold standard **SV** dataset by integrating
424 results from bulk PC3 DNA sequenced on multiple platforms (**ONT** PromethION,
425 **ONT** MinION, and Illumina HiSeq) and analyzed with multiple **SV** callers (Fig. 3a;
426 Extended Data Table 1). **SVs** detected by ≥ 2 callers on the same platform and sup-
427 ported by both long-read and short-read data were retained as gold-standard events,
428 ensuring high specificity across technologies.

429 Comparison against this gold standard revealed that unfiltered **WGA** data con-
430 tained extensive false-positive **SVs** (Fig. 3b,c). On PromethION, raw **WGA** data
431 produced 3.6 million **SV** calls, of which only 8,815 (0.24%) matched gold standard
432 events—indicating that over 99% were artifacts. After ChimeraLM filtering, total calls
433 dropped to 305,570 while retaining 8,067 true events, raising the validation rate to
434 2.64% (11-fold improvement) and preserving 91.5% of true variants. MinION data
435 showed similar results, with calls reduced from 451,390 to 38,432 and the validation
436 rate increasing from 1.59% to 16.3% (10-fold improvement) while retaining 87.2% of
437 true variants. These results highlight ChimeraLM’s ability to remove spurious **SV** calls
438 while maintaining biological sensitivity.

439 To complement this stringent validation, we next performed platform-matched bulk
440 validation, comparing **WGA**-derived **SV** calls against long-read bulk sequencing from
441 the same platform (Fig. 3d,e). This reference captures true **SVs** that may be missed by
442 short-read data, providing a more inclusive measure of recall. Under this benchmark,
443 ChimeraLM increased validation rates from 0.38% to 3.24% on PromethION (8.5-
444 fold improvement) and from 1.25% to 12.79% on MinION (10-fold improvement),
445 while retaining 71.9% and 87.1% of bulk-supported events, respectively. The consistent
446 improvements across independent datasets demonstrate that ChimeraLM effectively
447 suppresses **WGA**-induced artifacts without sacrificing detection of genuine **SVs**.

448 Together, these analyses demonstrate that ChimeraLM reduces false-positive **SV**
449 calls by 8–16 fold while preserving 72–92% of true variants, resulting in a substantial
450 enhancement of the signal-to-noise ratio in single-cell **SV** discovery. By restoring near-
451 bulk specificity and maintaining robust sensitivity, ChimeraLM enables more accurate
452 and interpretable downstream genomic analyses.

454 **ChimeraLM restores unbiased SV-type distributions and
455 characterizes artifact composition**

456 Amplification artifacts can distort the apparent spectrum of **SVs**, often inflating spe-
457 cific **SV** types. To evaluate whether ChimeraLM effectively corrects such distortions,
458
460

we compared **SV** type distributions across bulk, unfiltered **WGA**, and ChimeraLM-filtered datasets (Fig. 3f,g). Bulk sequencing showed relatively balanced proportions of **DELs**, **DUPs**, **INSSs**, **INVs**, and **TRAs**. In contrast, unfiltered **WGA** data exhibited a dramatic overrepresentation of **INVs** on both PromethION and MinION platforms, consistent with pervasive amplification artifacts. After ChimeraLM filtering, these distributions were largely restored toward bulk-like profiles: excessive **INVs** were markedly reduced while other **SV** categories remained stable. This shift reflects selective removal of artifact-supported **INVs** rather than indiscriminate loss of genuine inversion signals, demonstrating high specificity in distinguishing chimeric from biological reads.

To investigate the basis of this normalization, we analyzed **SV** calls supported exclusively by reads classified as chimeric by ChimeraLM (Fig. 3h,i). These artifact-supported events were overwhelmingly dominated by **INVs**, comprising 88.4% on PromethION and 92.4% on MinION. This pattern is consistent with template-switching junctions that produce inversion-like alignment signatures. Smaller fractions of **DELs** (5.1% and 3.8%), **DUPs** (3.4% and 2.4%), and **INSSs** (3.0% and 1.4%) were also observed, demonstrating that **WGA**-induced chimeras can mimic diverse **SV** categories rather than only **INVs**.

This characterization has important implications for single-cell genomics. Although **INVs** are the predominant artifact type, the coexistence of **DELs**, **DUPs**, and **INSSs** among chimeric events indicates that comprehensive filtering—rather than inversion-specific correction—is essential for accurate **SV** detection. Without ChimeraLM filtering, single-cell **SV** analyses would be confounded not only by false-positive **INVs** but also by other artifact-associated variants [31, 32]. By restoring biologically representative **SV** type distributions, ChimeraLM enables robust and interpretable characterization of structural variation in single cells without distortion from **WGA**-induced artifacts.

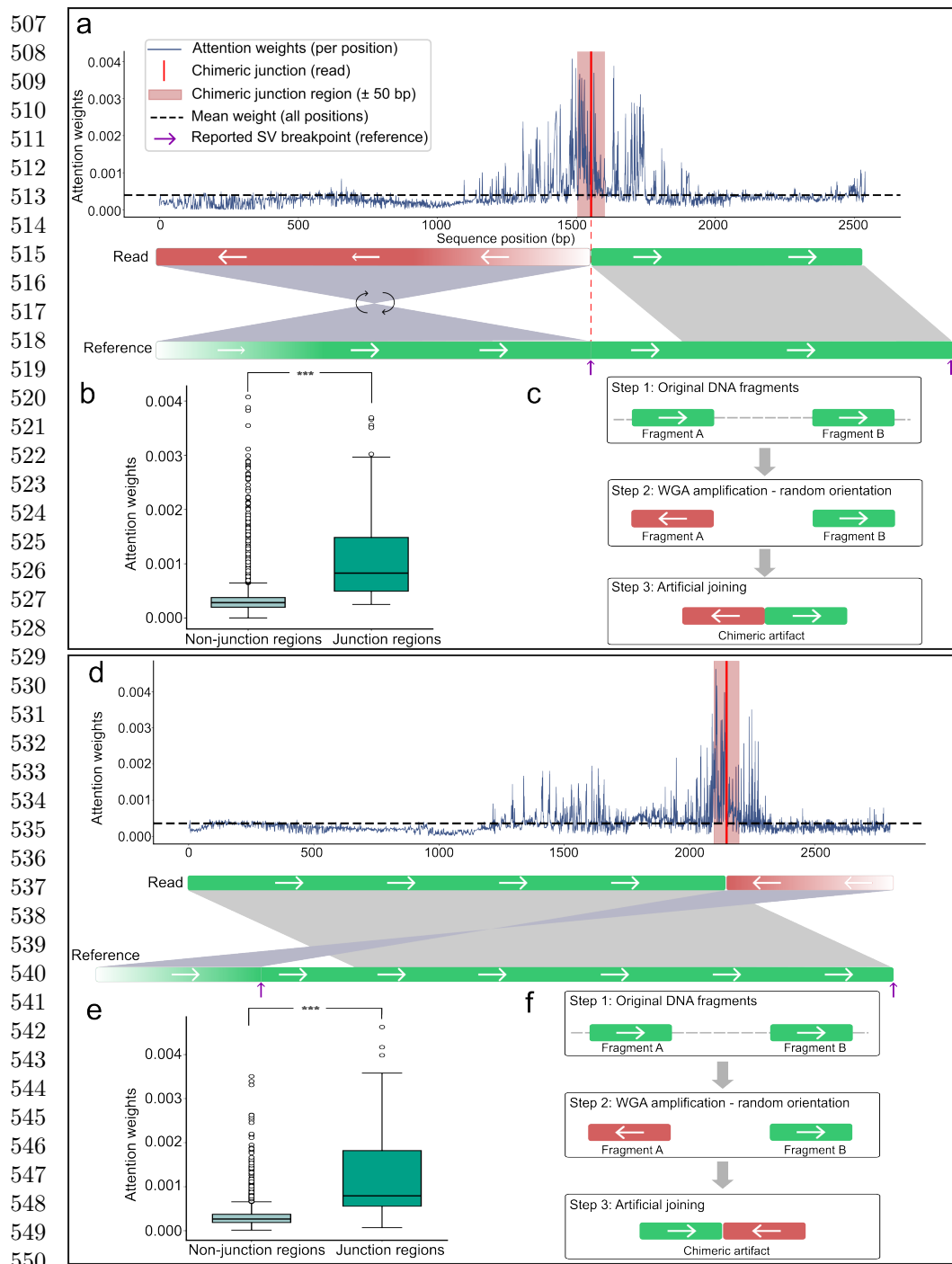


Fig. 4 ChimeraLM attention weights can localize to chimeric junction regions.

(a,d) Attention weight profiles for two representative chimeric reads. Upper panels show attention weights per sequence position (blue line) and mean attention (dashed line). Red vertical lines mark chimeric junction positions, with pink shading indicating junction region (± 50 bp). Purple arrows show reported SV breakpoints. Lower panels illustrate read alignments: reads (top bars) show orientation transitions at junctions (green = forward, red = reverse-complemented, arrows indicate strand), while reference genome (bottom bars) maintains continuous forward orientation. Gray regions connect aligned segments. (b,e) Quantitative attention analysis. Box plots show significantly elevated attention weights in junction region versus non-junction regions for both examples ($p = 5.3 \times 10^{-14}$ and $p = 6.8 \times 10^{-15}$, respectively; Wilcoxon rank-sum test). (c,f) Proposed chimera formation mechanisms. Step 1: Original DNA fragments from distant genomic loci exist in forward orientation. Step 2: During WGA, one or both fragments may undergo random reverse-complementation. Step 3: Template switching joins the fragments with discordant orientations, creating chimeric artifacts. The two examples illustrate different orientation patterns (forward-to-reverse vs reverse-to-forward transitions) arising from random strand selection during amplification.

ChimeraLM provides interpretable classification through attention visualization	553
	554
	555
	556
	557
	558
	559
	560
	561
	562
	563
	564
	565
	566
	567
	568
	569
	570
	571
	572
	573
	574
	575
	576
	577
	578
	579
	580
	581
	582
	583
	584
	585
	586
	587
	588
	589
	590
	591
	592
	593
	594
	595
	596
	597
	598
We next investigated whether ChimeraLM’s attention mechanism highlights biologically meaningful regions within sequencing reads (Fig. 4).	
For representative chimeric reads, attention weight profiles showed low baseline values across most positions but pronounced peaks at junction regions where template switching artificially joins DNA fragments from distinct genomic loci (Fig. 4a,d). These peaks coincided precisely with alignment breakpoints characterized by orientation changes between adjacent read segments—the defining signature of WGA-induced chimeric artifacts.	
Quantitative analysis confirmed that attention weights within junction regions (± 50 bp) were significantly higher than those in non-junction regions (Wilcoxon rank-sum test, $p = 5.3 \times 10^{-14}$ and $p = 6.8 \times 10^{-15}$) (Fig. 4b,e). Such localization indicates that ChimeraLM learns mechanistically relevant features associated with artificial junction formation rather than relying on spurious correlations.	
Schematic reconstruction of the amplification process further supports this interpretation (Fig. 4c,f). During WGA, DNA fragments from distant genomic loci may undergo random strand orientation changes before being joined by template switching. This process produces artificial junctions with discordant orientations—forward-to-reverse or reverse-to-forward—that generate inversion-like alignment signatures and are effectively recognized by the model’s attention peaks.	
Together, these analyses demonstrate that ChimeraLM’s attention mechanism can localize chimeric junctions at single-base resolution and capture the underlying orientation discontinuities that define WGA-induced artifacts.	
Discussion	579
WGA has enabled genomic analysis from single cells but introduces chimeric artifacts that compromise SV detection. ChimeraLM addresses this challenge through sequence-level classification of biological versus artificial reads, substantially improving SV calling accuracy before downstream analysis. This upstream filtering strategy—removing problematic sequences at the read level rather than correcting errors post hoc—provides a practical solution for single-cell genomics laboratories.	
Our results demonstrate several key advantages of ChimeraLM for long-read single-cell sequencing. The method achieves approximately 90% reduction in chimeric reads across nanopore platforms while retaining 87–92% of true SVs. It reduces false-positive SV calls by 8–16 fold, enabling researchers to focus on biologically relevant variants without manually filtering thousands of artifacts. Moreover, ChimeraLM performs consistently across PromethION and MinION without platform-specific retraining, indicating that it captures generalizable sequence features of WGA-induced chimeras. These results underscore the model’s robustness across diverse datasets and sequencing conditions.	
ChimeraLM’s effectiveness reflects the ability of deep learning models to capture complex sequence patterns that are difficult to encode in rule-based filters. Traditional quality control methods rely on predefined metrics such as mapping quality or read	

599 depth [23, 30], which may not effectively distinguish chimeric artifacts from biological reads. By learning directly from data, ChimeraLM discovers subtle compositional
600 and structural features that differentiate authentic genomic sequences from amplification artifacts. Furthermore, the model offers interpretability through attention
601 visualization, allowing researchers to examine which sequence regions drive classification.
602 Attention weights can concentrate sharply at junctions where template switching
603 joins DNA fragments from distinct loci, matching the known mechanism of chimera
604 formation. Some reads show more diffuse attention distributions, suggesting that
605 ChimeraLM integrates multiple complementary cues—such as junction orientation,
606 compositional biases, and local sequence context—to classify diverse artifact types.
607 This interpretability builds confidence in the model’s predictions and provides a lens
608 for probing the molecular processes underlying amplification-induced artifacts.

611 The improved reliability of **SV** detection has direct implications for single-cell
612 genomics. Studies of chromosomal instability, clonal evolution, and **SV** burden in
613 individual cells have long been constrained by high false-positive rates in **WGA**
614 data [31, 32]. ChimeraLM enables more confident identification of genuine **SVs**, sup-
615 porting research in cancer genomics, developmental biology, and aging where single-cell
616 resolution is essential for understanding cellular heterogeneity. Although the current
617 model processes reads independently, integrating additional contextual features—
618 such as coverage, mate-pair, or phasing information—could further enhance accuracy.
619 **Graphics Processing Unit (GPU)** resources are recommended for large-scale datasets,
620 while **Central Processing Unit (CPU)** inference remains feasible for smaller studies;
621 runtime optimization and model compression may improve accessibility for broader
622 use.

623 Future work should prioritize validation across diverse biological contexts in
624 long-read single-cell sequencing. Testing on multiple cell types (primary, stem, or
625 immune cells) and **WGA** protocols will establish generalizability. The interpretabil-
626 ity of attention-based models could also be leveraged to investigate mechanisms of
627 chimera formation: large-scale analysis of attention patterns may reveal recurrent
628 sequence motifs or genomic contexts associated with template switching, guiding the
629 development of improved amplification protocols. More broadly, ChimeraLM illus-
630 trates the potential of **GLMs** for data quality control applications [35]. Architectural
631 innovations such as the Hyena operator for efficient long-range modeling [39] may
632 have utility beyond chimera detection, addressing challenges such as contamination,
633 adapter artifacts, and systematic sequencing errors.

634 Looking ahead, ChimeraLM’s framework could extend beyond single-cell genomics
635 to address quality control challenges in other amplification-dependent technologies,
636 including cell-free DNA analysis, ancient DNA studies, and metagenomic sequencing
637 from low-biomass samples. The model’s interpretability through attention visual-
638 ization also opens opportunities for mechanistic studies of polymerase fidelity and
639 template-switching dynamics across different amplification protocols. Furthermore,
640 integration with emerging single-cell multi-omics platforms could enable simultaneous
641 quality control across genomic, transcriptomic, and epigenomic data layers, providing
642 a unified framework for artifact detection in complex single-cell experiments.

643
644

ChimeraLM thus provides a practical and interpretable framework for improving long-read single-cell genomic data quality. By removing WGA-induced chimeric artifacts at the read level and revealing the mechanistic features that drive them, the method not only enhances SV detection reliability but also deepens understanding of amplification-induced bias in single-cell genomics.

Methods

Cell culture, single-clone preparation, and nanopore sequencing

Cell culture and single-clone establishment

PC3 prostate cancer cells (ATCC® CRL-1435™) were cultured in RPMI-1640 medium supplemented with 10% fetal bovine serum and 1% penicillin–streptomycin at 37 °C with 5% CO₂. To minimize biological heterogeneity, a monoclonal population was established by serial dilution in 96-well plates, ensuring that each culture originated from a single cell. Mycoplasma contamination was routinely tested and confirmed negative prior to DNA extraction.

DNA extraction and whole-genome amplification

From the monoclonal population, two types of DNA samples were prepared: a bulk (non-amplified) control and ten single-cell MDA-amplified genomes. Bulk high-molecular-weight DNA was extracted using the Monarch® HMW DNA Extraction Kit for Cells & Blood (New England Biolabs). Individual cells were isolated using 1CellDish-60 mm (iBiochips) and amplified using the REPLI-g Advanced DNA Single Cell Kit (Qiagen) following the manufacturer's protocol. DNA concentration and fragment integrity were assessed with a Qubit 4 fluorometer and Agilent TapeStation (DNA 1000/5000 ScreenTape). Only samples meeting quality standards were used for library construction.

Nanopore library preparation and sequencing

Sequencing libraries were prepared using the ONT Ligation Sequencing Kit V14 (SQK-LSK114) and sequenced on MinION Mk1C or PromethION P2 Solo devices with R10.4.1 flow cells according to the manufacturer's genomic DNA workflow. Because all single-cell samples originated from the same monoclonal lineage, observed differences between amplified and bulk data primarily reflect MDA-induced artifacts rather than biological variation, providing a controlled experimental setting for downstream analyses.

Basecalling and read processing

Raw signal files (POD5) were basecalled using Dorado v0.5.0 with the high-accuracy model dna_r10.4.1_e8.2_400bps_hac@v4.3.0 [40]. Reads with mean quality < 10 or length < 500 bp were removed. Residual adapters and concatemers were trimmed using Cutadapt v4.0 [41] in two-pass error-tolerant mode. Cleaned reads were aligned to the GRCh38.p13 reference genome using minimap2 v2.26 (map-ont preset) [42]. Resulting BAM files were sorted and indexed with SAMtools v1.16 [43]. Read length

691 and mapping statistics were calculated using NanoPlot v1.46.1 [44]. All samples were
692 processed under identical parameters to ensure consistency across datasets.

693

694 *Chimeric read identification*

695 Chimeric reads were identified based on the presence of supplementary alignments in
696 BAM files using the [Supplementary Alignment \(SA\)](#) tag. The [SA](#) tag indicates that
697 a read has additional alignments beyond the primary alignment, which is character-
698 istic of chimeric sequences that map to multiple distant genomic locations. To ensure
699 accurate identification, we applied stringent filtering criteria: reads were classified as
700 chimeric only if they (1) were not unmapped, (2) contained the [SA](#) tag, (3) were not
701 secondary alignments, and (4) were not supplementary alignments themselves. This
702 filtering approach ensures that only primary alignments with supplementary mapping
703 evidence are considered chimeric, avoiding double-counting of the same chimeric event
704 and excluding low-quality or ambiguous alignments. Reads without the [SA](#) tag (single
705 continuous alignments) were classified as non-chimeric. This approach leverages the
706 standard BAM format specification to reliably identify reads with complex alignment
707 patterns.

708

709 **Training data construction**

710

711 *Data generation and sources*

712 To construct the training dataset, we generated [WGA](#) and bulk sequencing data from
713 PC3 cells. The [WGA](#) sample was amplified and sequenced on the PromethION P2 plat-
714 form ([ONT](#)), while three independent bulk datasets were produced from non-amplified
715 genomic DNA: bulk PromethION P2, bulk MinION Mk1c ([ONT](#)), and bulk PacBio.
716 These bulk datasets represent authentic biological sequences free from amplification-
717 induced artifacts. In contrast, [WGA](#) sequencing includes both genuine genomic reads
718 and artificial chimeras introduced during the amplification process. An additional
719 [WGA](#) dataset sequenced on the MinION Mk1c platform was reserved exclusively as
720 an independent test set for cross-platform evaluation.

721

722 *Ground truth annotation and class definition*

723 Ground truth labels were established by systematically comparing chimeric reads from
724 the [WGA](#) PromethION P2 dataset against those from the three bulk datasets. For
725 each [WGA](#) chimeric read, all alignment segments—defined by their genomic start
726 and end coordinates—were compared to the corresponding segments of bulk chimeric
727 reads. A [WGA](#) read was labeled as biological if every segment matched at least one
728 bulk chimeric read within a 1 kb positional tolerance, indicating that the structural
729 configuration is also present in non-amplified DNA. Reads lacking any matching pat-
730 tern across all bulk datasets were labeled as artificial chimeras, presumed to arise
731 from the amplification process. To ensure balanced class representation, additional
732 chimeric reads were randomly sampled from the bulk datasets and labeled as biologi-
733 cal, as these reads originate from genuine genomic rearrangements such as true [SVs](#).
734 The final labeled dataset combined the annotated [WGA](#) PromethION P2 reads with
735

736

the subsampled bulk chimeric reads and was subsequently partitioned into training,	737
validation, and test sets as described below.	738
	739
<i>Dataset partitioning and cross-platform validation</i>	740
The combined labeled dataset, derived from WGA PromethION P2 and bulk sequencing data, was divided into training (70%), validation (20%), and internal test (10%) sets using stratified random sampling to maintain class balance. These subsets were used respectively for model training, hyperparameter tuning, and performance evaluation on data from the same sequencing platform.	741
To evaluate cross-platform generalization, the complete WGA MinION Mk1c dataset was reserved as an independent external test set. This dataset, generated on a different nanopore platform, was never used during model training or internal testing. This two-level evaluation design allowed us to test whether ChimeraLM captures general sequence features of amplification-induced chimeras rather than platform-specific artifacts.	742
	743
	744
	745
	746
	747
	748
	749
	750
	751
	752
Model architecture	753
<i>Backbone encoder</i>	754
ChimeraLM employs the pre-trained HyenaDNA model [35] as its backbone encoder. This model was pre-trained on large-scale genomic data and provides robust sequence representations. DNA sequences are tokenized at single-nucleotide resolution, with each base (A, C, G, T, N) mapped to a unique integer token (7, 8, 9, 10, 11, respectively). Special tokens include [CLS]=0, [PAD]=4, and others for sequence processing. Input sequences are truncated at 32,768 bp or padded to enable batch processing.	755
For a tokenized input sequence $\mathbf{x} \in \mathbb{Z}^L$, the HyenaDNA backbone generates contextualized hidden representations:	756
$\mathbf{H} = \text{HyenaDNA}(\mathbf{x}) \in \mathbb{R}^{L \times 256}$	757
where $\mathbf{H} = (\mathbf{h}_1, \mathbf{h}_2, \dots, \mathbf{h}_L)$ represents position-wise hidden states with dimension 256. The Hyena operators [39] efficiently capture both local sequence motifs and long-range dependencies essential for distinguishing biological sequences from chimeric artifacts.	758
	759
	760
	761
	762
	763
	764
	765
	766
<i>Attention pooling</i>	767
To aggregate variable-length sequence representations into fixed-size vectors, ChimeraLM implements attention-based pooling. For hidden states $\mathbf{H} \in \mathbb{R}^{L \times 256}$, attention weights are computed through a two-layer network:	768
$\mathbf{e} = \text{GELU}(\text{Linear}_{256 \rightarrow 256}(\mathbf{H})) \in \mathbb{R}^{L \times 256}$	769
$\mathbf{s} = \text{Linear}_{256 \rightarrow 1}(\mathbf{e}) \in \mathbb{R}^{L \times 1}$	770
$\boldsymbol{\alpha} = \text{softmax}(\mathbf{s}) \in \mathbb{R}^{L \times 1}$	771
	772
	773
	774
	775
	776
	777
	778
	779
	780
	781
	782

783 The pooled representation is the weighted sum of hidden states:
 784
 785
$$\mathbf{h}_{\text{pooled}} = \sum_{i=1}^L \alpha_i \mathbf{h}_i \in \mathbb{R}^{256}$$

 786
 787 This mechanism assigns learned importance weights to each sequence position,
 788 enabling the model to focus on informative regions while accommodating natural
 789 variability in read lengths.
 790
 791
 792 ***Classification head***
 793
 794 The pooled representation is processed through a **MLP** with residual connections. The
 795 first layer expands dimensionality:
 796
 797
$$\mathbf{f}_1 = \text{Dropout}_{0.1}(\text{GELU}(\text{Linear}_{256 \rightarrow 512}(\mathbf{h}_{\text{pooled}}))) \in \mathbb{R}^{512}$$

 798
 799 Subsequent residual blocks with input $\mathbf{f}_{\text{in}} \in \mathbb{R}^{512}$ compute:
 800
 801
$$\mathbf{f}_{\text{out}} = \text{Dropout}_{0.1}(\text{Linear}_{512 \rightarrow 512}(\text{GELU}(\text{Linear}_{512 \rightarrow 512}(\mathbf{f}_{\text{in}})))) + \mathbf{f}_{\text{in}}$$

 802 where the skip connection enables stable gradient flow during training. The final layer
 803 produces binary classification logits:
 804
 805
$$\mathbf{z} = [z_0, z_1] = \text{Linear}_{512 \rightarrow 2}(\mathbf{f}_{\text{final}}) \in \mathbb{R}^2$$

 806
 807 where z_0 and z_1 represent logits for biological and artificial chimeric classes, respec-
 808 tively. During inference, the predicted class is $\hat{y} = \text{argmax}_{i \in \{0,1\}} z_i$.
 809
 810
 811 ***Model summary***
 812 The complete ChimeraLM pipeline processes DNA sequences through: (1) single-
 813 nucleotide tokenization, (2) HyenaDNA backbone encoding to generate contextualized
 814 representations, (3) attention pooling to aggregate position-specific features, (4) **MLP**
 815 layers with residual connections to learn classification features, and (5) binary classi-
 816 fication output. The entire model is trained end-to-end using labeled **WGA** and bulk
 817 sequencing data.
 818
 819 **Model training and optimization**
 820
 821 ***Training configuration***
 822 ChimeraLM was trained using PyTorch [45] and PyTorch Lightning [46] frameworks.
 823 Input sequences were tokenized using the tokenizer with maximum sequence length of
 824 32,768 bp. Sequences longer than this threshold were truncated; shorter sequences were
 825 padded to enable batch processing. Training employed mixed-precision computation
 826 (bf16) to accelerate training while maintaining numerical stability.
 827
 828

Optimization procedure	829
We used the AdamW optimizer [47] with learning rate $\eta = 1 \times 10^{-4}$ and weight decay $\lambda = 0.01$. AdamW implements adaptive learning rates with decoupled weight decay, combining the benefits of Adam optimization with proper L2 regularization. A ReduceLROnPlateau scheduler dynamically adjusted the learning rate based on validation loss, reducing it by a factor of 0.1 when no improvement occurred for 10 consecutive epochs. Early stopping with patience of 10 epochs prevented overfitting by terminating training when validation performance plateaued. A fixed random seed (12345) ensured reproducibility across training runs.	830 831 832 833 834 835 836 837

The training objective used cross-entropy loss for binary classification. For a training example with true class label $y \in \{0, 1\}$ and model logits $\mathbf{z} = [z_0, z_1]$, the loss is:

$$\mathcal{L}(\mathbf{z}, y) = -\log \left(\frac{\exp(z_y)}{\exp(z_0) + \exp(z_1)} \right) = -z_y + \log(\exp(z_0) + \exp(z_1))$$

where z_0 and z_1 represent logits for biological and artificial chimeric classes, respectively.

Training implementation

Training used batch size of 16 sequences with 30 parallel data loading workers. GPU acceleration was employed for efficient processing, with training typically requiring 96–120 hours depending on dataset size. Model checkpointing saved the best-performing model based on validation metrics. Configuration management used Hydra [48] to enable reproducible experimentation.

Model evaluation

Performance was monitored using accuracy, precision, recall, and F1 score on the validation set after each epoch:

$$\text{Precision} = \frac{\text{TP}}{\text{TP} + \text{FP}}, \quad \text{Recall} = \frac{\text{TP}}{\text{TP} + \text{FN}}$$

$$\text{F1} = \frac{2 \times \text{Precision} \times \text{Recall}}{\text{Precision} + \text{Recall}}, \quad \text{Accuracy} = \frac{\text{TP} + \text{TN}}{\text{TP} + \text{TN} + \text{FP} + \text{FN}}$$

where TP (true positives) are chimeric reads correctly classified as artificial, TN (true negatives) are biological reads correctly classified as biological, FP (false positives) are biological reads misclassified as artificial, and FN (false negatives) are chimeric reads misclassified as biological. Final model selection was based on best validation performance as determined by early stopping.

Model inference and application

Inference pipeline

To apply ChimeralLM to new WGA sequencing data, the model takes a BAM file as input. Chimeric reads are identified using SA tags and filtered to exclude unmapped, secondary, or supplementary alignments. Each chimeric read sequence is tokenized

875 using the tokenizer (maximum length 32,768 bp, with truncation or padding as
876 needed). The trained model processes sequences in batches, generating two logits
877 $[z_0, z_1]$ for each read corresponding to biological and artificial chimeric classes. Clas-
878 sification is determined by $\hat{y} = \text{argmax}(z_0, z_1)$. ChimeraLM outputs a filtered BAM
879 file containing only reads classified as biological, which can be directly used for
880 downstream analyses including **SV** calling.

881

882 Performance evaluation

883

884 Test set evaluation

885 Final model performance was evaluated on the held-out test set and the independent
886 MinION Mk1c dataset. Metrics (precision, recall, F1 score, accuracy) were computed
887 as described in the training section, where true positives represent chimeric reads
888 correctly classified as artificial and true negatives represent biological reads correctly
889 classified as biological.

890

891 SV calling

892 **SVs** were called using multiple tools to ensure comprehensive detection. For long-
893 read data (ONT PromethION P2 and MinION Mk1c), we used Sniffles v2.5 [24, 25],
894 DeBreak v1.2 [26], SVIM v2.0.0 [27], and cuteSV v2.1.1 [28]. For short-read data of the
895 PC3 cell line, we used both the CCLE Illumina whole-genome sequencing dataset and
896 the PRJNA361315 Illumina WGS dataset, processed with Manta v1.6.0 [49], DELLY
897 v1.5.0 [50], and SvABA v1.1.0 [51]. All tools were executed with default recommended
898 parameters.

899

900 Gold standard SV dataset construction

901 A high-confidence gold standard **SV** dataset was generated from bulk PC3 sequencing
902 data to evaluate the impact of ChimeraLM on **SV** detection accuracy (Fig. 3a). All
903 **SV** comparison and breakpoint correction were performed using OctopuSV v0.2.3 [52].
904 We used four datasets: bulk MinION Mk1c, bulk PromethION P2, the CCLE Illumina
905 WGS dataset, and the PRJNA361315 Illumina WGS dataset. Within each dataset, **SV**
906 events supported by at least two independent callers were retained. Variants supported
907 by two or more datasets were designated as gold standard **SVs** for benchmarking.
908

909

910 SV benchmarking analysis

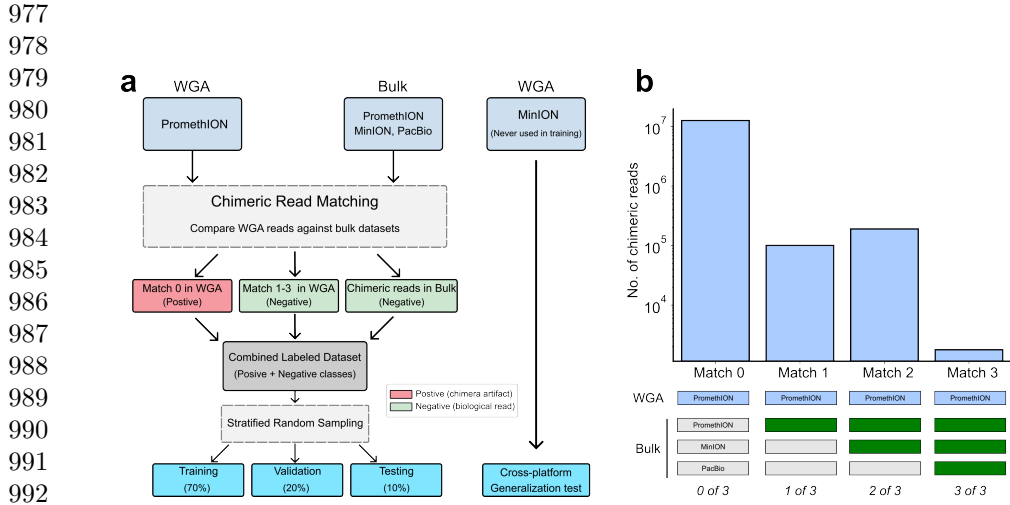
911

912 To assess the impact of ChimeraLM on **SV** calling accuracy, we compared **SV** calls from
913 unfiltered **WGA** data and ChimeraLM-filtered **WGA** data against two references: (1)
914 the stringent multi-platform gold standard dataset, and (2) platform-matched long-
915 read bulk sequencing data. Benchmarking was performed using Truvari v4.2.2 [53]
916 with default parameters. **SVs** were considered supported if they matched reference
917 variants within the defined breakpoint tolerance. Validation rates were calculated as
918 the proportion of called **SVs** supported by the reference. This dual benchmarking
919 strategy quantifies both improvements in detecting high-confidence multi-platform
920 **SVs** and the retention of platform-specific true variants.

Benchmarking against existing methods	921
ChimeraLM was compared to two existing computational methods for detecting amplification-induced chimeric artifacts: SACRA [30] (GitHub commit 9a2607e) and 3rd-ChimeraMiner [23] (GitHub commit 04b5233). Both tools were applied to WGA data from PromethION P2 and MinION Mk1c platforms using default parameters as recommended in their documentation. Performance was evaluated by measuring the percentage reduction in chimeric reads relative to unprocessed WGA data. Chimeric reads were identified using WGA tag-based alignment criteria (reads with SA tags indicating split alignments), and reduction rates were calculated as the proportion of chimeric reads removed by each method.	922 923 924 925 926 927 928 929 930 931 932 933 934 935 936 937 938 939 940 941 942 943 944 945 946 947 948 949 950 951 952 953 954 955 956 957 958 959 960 961 962 963 964 965 966
Attention weight analysis	933
To investigate ChimeraLM’s interpretability, we analyzed attention weights from the pooling mechanism for representative chimeric reads. Attention weights indicate the relative importance assigned to each sequence position during classification. For selected reads, we extracted per-position attention weights and visualized them alongside read alignments to identify whether the model focuses on mechanistically relevant regions.	934 935 936 937 938 939 940 941 942 943 944 945 946 947 948 949 950 951 952 953 954 955 956 957 958 959 960 961 962 963 964 965 966
Chimeric junction positions were identified from alignment data (defined by breakpoints in SA tags). A window of ± 50 bp surrounding each junction was designated as the junction region. Attention weights within junction region were compared to non-junction regions using the Wilcoxon rank-sum test [54], with statistical significance assessed at $p < 0.001$.	940 941 942 943 944 945 946 947 948 949 950 951 952 953 954 955 956 957 958 959 960 961 962 963 964 965 966
Data visualization	946
Figures were generated using Python with Matplotlib [55] and Seaborn [56].	947 948 949 950 951 952 953 954 955 956 957 958 959 960 961 962 963 964 965 966
Computing resources	950
Computations were performed on a High Performance Computing (HPC) server with 64-core Intel Xeon Gold 6338 CPU, 256 GB RAM, and two NVIDIA A100 GPUs (80 GB memory each).	951 952 953 954 955 956 957 958 959 960 961 962 963 964 965 966
Supplementary information.	955
Acknowledgements. We thank Tingyou Wang for guidance on figure preparation. This project was supported in part by NIH grants R35GM142441 and R01CA259388 awarded to RY.	956 957 958 959 960 961 962 963 964 965 966
Declarations	961
Author Contributions. YL, QG and RY designed the study. YL and QG performed the analysis. QG performed the experiments. YL and QG designed and implemented the model. YL built the command-line tool and documentation. YL, QG and RY wrote the manuscript. RY supervised this work.	962 963 964 965 966

967
968 **Extended Data Table 1** Sequencing and alignment statistics of PC3

Sample	Platform	Reads ($\times 10^6$)	Total bases (Gb)	Total aligned bases (Gb)	Fraction aligned	Mean length (bp)	Mean quality (Q)	Average identity (%)
WGA	MinION	9.11	14.6	10.4	0.7	1,603	14.3	97.6
WGA	PromethION	44.69	128.2	69.2	0.5	2,869	14.5	96.1
Bulk	MinION	0.97	8.1	7.1	0.9	8,310	17.2	97.3
Bulk	PromethION	8.00	69.9	62.4	0.9	8,732	18.5	97.7



994 **Extended Data Fig. 1 Training dataset construction and ground-truth labeling strategy**
995 **for PC3 cell line.** (a) Schematic workflow for generating labeled training data. **WGA** PromethION
996 data containing both biological and artificial chimeric reads is compared against three independent
997 bulk sequencing datasets from the same cell line (PromethION, MinION, and PacBio platforms).
998 Chimeric reads are classified through systematic matching: reads with no matches across all bulk
999 datasets (Match 0) are labeled as artificial chimeras (positive class, red); reads matching one or
1000 more bulk datasets (Match 1–3) are labeled as biological reads (negative class, green), along with
1001 chimeric reads sampled directly from bulk data. The combined labeled dataset undergoes stratified
1002 random sampling to generate training (70%), validation (20%), and testing (10%) sets for model
1003 development. The **WGA** MinION dataset is reserved as an independent cross-platform generalization
1004 test set. (b) Distribution of chimeric read matches between **WGA** and bulk sequencing datasets. Bar
1005 chart showing the number of chimeric reads (y-axis, log scale) grouped by how many bulk datasets (x-
1006 axis) contained matching chimeric structures when comparing **WGA** PromethION reads against bulk
1007 sequencing data. “Match 0” indicates reads with no matches in any bulk dataset (classified as artificial
1008 chimeras, $\sim 10^7$ reads), whereas “Match 1–3” indicate reads with matches in one, two, or all three
1009 bulk datasets (classified as biological reads, $\sim 10^5$ reads each). Color-coded boxes below bars indicate
1010 which bulk platforms validated each read category: PromethION (light blue), MinION (white), and
1011 PacBio (white); green boxes indicate platform-specific validation. The substantial imbalance between
1012 Match 0 ($\sim 10^7$) and Match 1–3 categories ($\sim 10^5$ each) reflects the high prevalence of **WGA**-induced
1013 artifacts, necessitating balanced subsampling for supervised learning.

1014
1015 **Data Availability.** The raw sequencing data generated in this study have been
1016 deposited in the NCBI Sequence Read Archive (SRA) under BioProject accession

PRJNA1354861. The dataset includes Oxford Nanopore long-read whole-genome sequencing of PC3 prostate cancer cells and MDA-amplified single-cell derivatives. The individual SRA accessions are as follows: PC3 bulk (MinION Mk1C), SRR35904028; PC3 bulk (PromethION P2), SRR35904029; PC3 10-cell WGA (MinION Mk1C), SRR35904026; PC3 10-cell WGA (PromethION P2), SRR35904027. We can access the data at the following link: https://dataview.ncbi.nlm.nih.gov/object/PRJNA1354861?reviewer=viej6cv6mgbli3n7a9a5k1bsb3	1013 1014 1015 1016 1017 1018 1019 1020 1021 1022 1023 1024 1025 1026 1027 1028 1029 1030 1031 1032 1033 1034 1035 1036 1037 1038 1039 1040 1041 1042 1043 1044 1045 1046 1047 1048 1049 1050 1051 1052 1053 1054 1055 1056 1057 1058
Code Availability. ChimeraLM, implemented in Python, is open source and available on GitHub (https://github.com/ylab-hi/ChimeraLM) under the Apache License, Version 2.0. The package can be installed via PyPI (https://pypi.org/project/chimeralm) using pip, with wheel distributions provided for Windows, Linux, and macOS to ensure easy cross-platform installation. An interactive demo is available on Hugging Face (https://huggingface.co/spaces/yangliz5/ChimeraLM), allowing users to test DeepChopper's functionality without local installation. For large-scale analyses, we recommend using ChimeraLM on systems with GPU acceleration. Detailed system requirements and optimization guidelines are available in the repository's documentation (https://ylab-hi.github.io/ChimeraLM/).	
Conflict of interest. RY has served as an advisor/consultant for Tempus AI, Inc. This relationship is unrelated to and did not influence the research presented in this study.	
Acronyms	
CPU Central Processing Unit 14	1037
DEL deletion 9, 11	1038
dMDA droplet-based MDA 2	1039
DOP-PCR Degenerate Oligonucleotide-Primed PCR 2	1040
DUP duplication 9, 11	1041
GLM Genomic Language Model 4, 14	1042
GPU Graphics Processing Unit 14, 19, 21, 23	1043
HPC High Performance Computing 21	1044
INS insertion 9, 11	1045
INV inversion 1, 9, 11	1046
LIANTI Linear Amplification via Transposon Insertion 2	1047
MALBAC Multiple Annealing and Looping-based Amplification Cycles 2	1048
MDA Multiple Displacement Amplification 2, 3	1049
MLP multilayer perceptron 5, 6, 18	1050
ONT Oxford Nanopore Technologies 4, 9, 10, 15, 16	1051

1059 **PTA** Primary Template-directed Amplification 2

1060

1061 **SA** Supplementary Alignment 16, 19, 21

1062 **SV** Structural Variation 1–5, 9–16, 20

1063

1064 **TRA** translocation 9, 11

1065 **WGA** Whole Genome Amplification 1–22

1066

1067

1068 **References**

1069 [1] Kalf-Ezra, E. *et al.* Single-cell somatic copy number variants in brain using
1070 different amplification methods and reference genomes. *Communications Biology*
1071 1288 (2024).

1073 [2] Sun, C. *et al.* Mapping recurrent mosaic copy number variation in human neurons.
1074 *Nature Communications* 4220 (2024).

1076 [3] Navin, N. *et al.* Tumour evolution inferred by single-cell sequencing. *Nature* **472**,
1077 90–94 (2011).

1078

1079 [4] Macaulay, I. C. & Voet, T. Single cell genomics: Advances and future perspectives.
1080 *PLOS Genetics* **10**, e1004126 (2014).

1081

1082 [5] Leung, M. L. *et al.* Highly multiplexed targeted dna sequencing from single nuclei.
1083 *Nature Protocols* 214–235 (2016).

1084

1085 [6] Gawad, C., Koh, W. & Quake, S. R. Single-cell genome sequencing: current state
1086 of the science. *Nature Reviews Genetics* 175–188 (2016).

1087

1088 [7] Chen, C. *et al.* Single-cell whole-genome analyses by linear amplification via
1089 transposon insertion (LIANTI). *Science (new York, N.Y.)* **356**, 189–194 (2017).

1090

1091 [8] Zong, C., Lu, S., Chapman, A. R. & Xie, X. S. Genome-wide detection of single-
1092 nucleotide and copy-number variations of a single human cell. *Science* 1622–1626
1093 (2012).

1094

1095 [9] Huang, L., Ma, F., Chapman, A., Lu, S. & Xie, X. S. Single-cell whole-genome
1096 amplification and sequencing: methodology and applications. *Annual Review of
Genomics and Human Genetics* 79–102 (2015).

1097

1098 [10] Dean, F. B. *et al.* Comprehensive human genome amplification using multiple
1099 displacement amplification. *Proceedings of the National Academy of Sciences* **99**,
1100 5261–5266 (2002).

1101

1102 [11] Lasken, R. S. & Stockwell, T. B. Mechanism of chimera formation during the
1103 multiple displacement amplification reaction. *BMC Biotechnology* **7**, 19 (2007).

1104

- [12] Pinard, R. *et al.* Assessment of whole genome amplification-induced bias through high-throughput, massively parallel whole genome sequencing. *BMC Genomics* **7**, 216 (2006). 1105
1106
1107
1108
1109
1110
1111
1112
1113
1114
1115
1116
1117
- [13] Telenius, H. *et al.* Degenerate oligonucleotide-primed PCR: General amplification of target DNA by a single degenerate primer. *Genomics* **13**, 718–725 (1992). 1108
1109
1110
1111
1112
1113
1114
1115
1116
1117
- [14] Gonzalez-Pena, V. *et al.* Accurate genomic variant detection in single cells with primary template-directed amplification. *Proceedings of the National Academy of Sciences* **118**, e2024176118 (2021). 1111
1112
1113
1114
1115
1116
1117
- [15] Hård, J. *et al.* Long-read whole-genome analysis of human single cells. *Nature Communications* **14**, 5164 (2023). 1115
1116
1117
- [16] Dippenaar, A. *et al.* Droplet based whole genome amplification for sequencing minute amounts of purified mycobacterium tuberculosis DNA. *Scientific Reports* **14**, 9931 (2024). 1118
1119
1120
1121
- [17] de Bourcy, C. F. A. *et al.* A quantitative comparison of single-cell whole genome amplification methods. *PLoS ONE* e105585 (2014). 1122
1123
1124
- [18] Biezuner, T. *et al.* Comparison of seven single cell whole genome amplification commercial kits using targeted sequencing. *Scientific Reports* 17171 (2021). 1125
1126
1127
- [19] Fu, Y. *et al.* Uniform and accurate single-cell sequencing based on emulsion whole-genome amplification. *Proceedings of the National Academy of Sciences* 11923–11928 (2015). 1128
1129
1130
1131
1132
1133
1134
- [20] Agyabeng-Dadzie, F. *et al.* Evaluating the benefits and limits of multiple displacement amplification with whole-genome oxford nanopore sequencing. *Molecular Ecology Resources* e14094 (2025). 1135
1136
1137
1138
- [21] Dean, F. B., Nelson, J. R., Giesler, T. L. & Lasken, R. S. Rapid amplification of plasmid and phage DNA using Phi29 DNA polymerase and multiply-primed rolling circle amplification. *Genome Research* **11**, 1095–1099 (2001). 1139
1140
1141
1142
- [22] Lu, N., Qiao, Y., Lu, Z. & Tu, J. Chimera: The spoiler in multiple displacement amplification. *Computational and Structural Biotechnology Journal* 1688–1696 (2023). 1143
1144
1145
1146
- [23] Lu, N. *et al.* Exploration of whole genome amplification generated chimeric sequences in long-read sequencing data. *Briefings in Bioinformatics* **24**, bbad275 (2023). 1147
1148
1149
1150

- 1151 [25] Smolka, M. *et al.* Detection of mosaic and population-level structural variants
1152 with sniffles2. *Nature Biotechnology* 1571–1580 (2024).
- 1153
- 1154 [26] Chen, Y. *et al.* Deciphering the exact breakpoints of structural variations using
1155 long sequencing reads with DeBreak. *Nature Communications* 283 (2023).
- 1156
- 1157 [27] Heller, D. & Vingron, M. SVIM: Structural variant identification using mapped
1158 long reads. *Bioinformatics* 2907–2915 (2019).
- 1159
- 1160 [28] Jiang, T. *et al.* Long-read-based human genomic structural variation detection
1161 with cuteSV. *Genome Biology* 189 (2020).
- 1162
- 1163 [29] Alkan, C., Coe, B. P. & Eichler, E. E. Genome structural variation discovery and
1164 genotyping. *Nature Reviews Genetics* 12, 363–376 (2011).
- 1165
- 1166 [30] Kiguchi, Y., Nishijima, S., Kumar, N., Hattori, M. & Suda, W. Long-read
1167 metagenomics of multiple displacement amplified DNA of low-biomass human gut
1168 phageomes by SACRA pre-processing chimeric reads. *DNA Research* 28, dsab019
1169 (2021).
- 1170
- 1171 [31] Kosugi, S. *et al.* Comprehensive evaluation of structural variation detection
1172 algorithms for whole genome sequencing. *Genome Biology* 20, 117 (2019).
- 1173
- 1174 [32] Mahmoud, M. *et al.* Structural variant calling: The long and the short of it.
1175 *Genome Biology* 20, 246 (2019).
- 1176
- 1177 [33] Dalla-Torre, H. *et al.* Nucleotide transformer: building and evaluating robust
1178 foundation models for human genomics. *Nature Methods* 287–297 (2025).
- 1179
- 1180 [34] Zhou, Z. *et al.* DNABERT-2: Efficient foundation model and benchmark for
1181 multi-species genomes, 1–24 (OpenReview.net, 2024).
- 1182
- 1183 [35] Nguyen, E. *et al.* HyenaDNA: Long-range genomic sequence modeling at single
1184 nucleotide resolution, Vol. 36, 43177–43201 (Curran Associates, Inc., 2023).
- 1185
- 1186 [36] Consens, M. E. *et al.* To transformers and beyond: Large language models for
1187 the genome (2023). [arXiv:2311.07621](https://arxiv.org/abs/2311.07621).
- 1188
- 1189 [37] Routhier, E. & Mozziconacci, J. Genomics enters the deep learning era. *PeerJ*
1190 10, e13613 (2022).
- 1191
- 1192 [38] Li, Y. *et al.* A genomic language model for chimera artifact detection in nanopore
1193 direct rna sequencing. *bioRxiv* (2024). URL <https://www.biorxiv.org/content/early/2024/10/25/2024.10.23.619929>.
- 1194
- 1195 [39] Poli, M. *et al.* Hyena hierarchy: Towards larger convolutional language models,
1196 Vol. 202, 28043–28078 (PMLR, 2023).

- [40] PLC., O. N. Dorado. <https://github.com/nanoporetech/dorado> (2023). 1197
1198
- [41] Martin, M. Cutadapt removes adapter sequences from high-throughput sequencing reads. *Embojournal* **17**, 10–12 (2011). 1199
1200
- [42] Li, H. Minimap2: Pairwise alignment for nucleotide sequences. *Bioinformatics* 3094–3100 (2018). 1201
1202
- [43] Danecek, P. *et al.* Twelve years of SAMtools and BCFtools. *GigaScience* giab008 (2021). 1203
1204
- [44] De Coster, W. & Rademakers, R. NanoPack2: Population-scale evaluation of long-read sequencing data. *Bioinformatics* **39**, btad311 (2023). 1205
1206
- [45] Paszke, A. *et al.* *PyTorch: An imperative style, high-performance deep learning library*, Vol. 32, 8024–8035 (Curran Associates, Inc., 2019). 1207
1211
1212
- [46] Falcon, W. & The PyTorch Lightning team. PyTorch Lightning. GitHub repository (2019). URL <https://github.com/Lightning-AI/lightning>. 1213
1214
- [47] Loshchilov, I. & Hutter, F. *Decoupled weight decay regularization* (2019). 1215
1216
- [48] Yadan, O. Hydra - a framework for elegantly configuring complex applications. GitHub repository (2019). URL <https://github.com/facebookresearch/hydra>. 1217
1218
1219
- [49] Chen, X. *et al.* Manta: Rapid detection of structural variants and indels for germline and cancer sequencing applications. *Bioinformatics* 1220–1222 (2016). 1220
1221
1222
- [50] Rausch, T. *et al.* DELLY: Structural variant discovery by integrated paired-end and split-read analysis. *Bioinformatics* i333–i339 (2012). 1223
1224
1225
- [51] Wala, J. A. *et al.* SvABA: Genome-wide detection of structural variants and indels by local assembly. *Genome Research* 581–591 (2018). 1226
1227
1228
- [52] Guo, Q., Li, Y., Wang, T.-Y., Ramakrishnan, A. & Yang, R. OctopusV and TentacleSV: A one-stop toolkit for multi-sample, cross-platform structural variant comparison and analysis. *Bioinformatics* btaf599 (2025). 1229
1230
1231
- [53] English, A. C., Menon, V. K., Gibbs, R. A., Metcalf, G. A. & Sedlazeck, F. J. Truvari: Refined structural variant comparison preserves allelic diversity. *Genome Biology* **23**, 271 (2022). 1232
1233
1234
1235
- [54] Virtanen, P. *et al.* SciPy 1.0: Fundamental algorithms for scientific computing in python. *Nature Methods* 261–272 (2020). 1236
1237
1238
- [55] Hunter, J. D. Matplotlib: A 2d graphics environment. *Computing in Science & Engineering* 90–95 (2007). 1239
1240
1241
1242

1243 [56] Waskom, M. L. seaborn: statistical data visualization. *Journal of Open Source*
1244 *Software* 3021 (2021).
1245
1246
1247
1248
1249
1250
1251
1252
1253
1254
1255
1256
1257
1258
1259
1260
1261
1262
1263
1264
1265
1266
1267
1268
1269
1270
1271
1272
1273
1274
1275
1276
1277
1278
1279
1280
1281
1282
1283
1284
1285
1286
1287
1288